Available online at www.sciencedirect.com
ScienceDirect
Acta Materialia 56 (2008) 4890–4895
Acta MATERIALIA
www.elsevier.com/locate/actamat

Coercivity enhancement in boron-enriched stoichiometric REFeB melt-spun alloys

I. Betancourt [a,*], G. Cruz-Arcos [a], T. Schrefl [b], H.A. Davies [b]

[a] Departamento de Materiales Metálicos y Cerámicos, Instituto de Investigaciones en Materiales, Universidad Nacional Autónoma de México, 04510 México, D.F., Mexico
[b] Department of Engineering Materials, University of Sheffield, Sir Robert Hadfield Building, Mappin Street, Sheffield S1 3JD, UK

Received 6 March 2008; received in revised form 26 April 2008; accepted 4 June 2008
Available online 14 July 2008

Abstract

Considerable enhancement of magnetic properties was attained in initially stoichiometric nanophase $RE_{12}Fe_{82}B_6$ melt-spun alloys (RE = Nd, Nd + Pr) by means of an excess B content (10 at%) and additions of Zr and Co (2% and 7%, respectively). The intrinsic coercivity exhibited a marked improvement (with respect to the stoichiometric 6 at% B alloy), within the range 50–65%, with a maximum of 1161 ± 14 kA m^{-1} for the B-rich and Zr-containing alloy, together with an excellent combination of remanence and energy density values of 0.90 ± 0.01 T and 137 ± 4 kJ m^{-3}, respectively. Further Co addition led to a Curie temperature increase, while preserving high coercivity (1176 ± 31 kA m^{-1}) and useful energy densities (119 ± 4 kJ m^{-3}). Results were interpreted on the basis of alloy microstructural features and on variations of the intrinsic magnetic properties, supported by micromagnetic calculations.

Keywords: Nanocrystalline materials; Hard magnets; Coercivity; Micromagnetism

1. Introduction

Rare earth (RE)–iron–boron hard magnetic alloys have been the subject of intense study since their first announcement in 1984 [1,2] due to their outstanding combination of magnetic properties such as: high intrinsic coercivity $_iH_c$ (300–1500 kA m^{-1}, depending on RE content) and high maximum energy densities $(BH)_{max}$ (between 100 and 170 kJ m^{-3} for isotropic alloys) [3–5]. These alloys are the precursor materials for fabrication of permanent magnets, which can be used for a very wide range of applications: loudspeakers, uniform and non-uniform magnetic field sources, magnetic separation, magnetic bearings and couplings, levitation systems, actuators, sensors (anisotropic magnets), motors (dc, synchronous, stepping: isotropic magnets) and more recently, for biomedical devices, such as: cardiac valves, magnetic catheters, dental care and for "magnetotherapy" [6–9].

It is well established that the microstructure and magnetic properties of RE–Fe–B alloys are very sensitive to both the alloy composition and the processing parameters [3–6,9,10]. For melt-spun alloys, the stoichiometric composition (with RE content ~11.7 at%) results in isotropic alloys with a microstructure comprising uniaxial, randomly oriented crystallites and typical magnetic properties of $_iH_c$ between 700 and 800 kA m^{-1} and $(BH)_{max}$ within the range 110–170 kJ m^{-3} [3–5,9] (depending on the remanence J_r values, since $(BH)_{max}$ is approximately proportional to J_r^2 for materials with $\mu_{oi}H_c > J_r/2$ [11,12]). Reduction in the mean grain size d_g leads to an increasing degree of exchange interaction between magnetic moments on adjacent grains surface, which in turn leads to enhanced J_r values (well above the $0.5J_s$ limit expected for non-interacting, uniaxial, randomly oriented particles), though accompanied by reduced coercivities [3–5,9,13]. On the other hand, mixed rare-earth Nd–Pr–Fe–B based nanocomposite magnets are of interest because of the larger anisotropy constant K_1 for the $Pr_2Fe_{14}B$ phase than for its Nd counterpart (which results in higher $_iH_c$ values [3,9,14–

* Corresponding author. Tel.: +52 55 56224654; fax: +52 55 56161371.
E-mail address: israelb@correo.unam.mx (I. Betancourt).

1359-6454/$34.00
doi:10.1016/j.actamat.2008.06.013

16]) and the absence of the spin reorientation phenomenon in $Pr_2Fe_{14}B$ [6,11–15], in addition to the potential economic benefit (i.e., lower cost) of employing didymium having Nd:Pr ratios that correspond to those that occur naturally in rare-earth ores (typically 3–4:1) [17]. In the present work, we report and discuss the effects of excess B and of Zr–Co additions on the magnetic properties of initially stoichiometric, isotropic melt-spun (NdPr)–Fe–B alloys.

2. Experimental details

Initial alloy ingots having compositions $Nd_2Fe_{82}B_6$, $RE_{12}Fe_{82}B_6$, $RE_{12}Fe_{78}B_{10}$, $RE_{12}Fe_{76}Zr_2B_{10}$ and $RE_{12}(Fe_{0.9}Co_{0.1})_{76}Zr_2B_{10}$ ($RE = Nd_{0.75}Pr_{0.25}$), were prepared using commercial-grade materials by arc-melting the constituents in a Ti-gettered, high-purity Ar atmosphere. Nanocrystalline alloy samples were obtained by a devitrification annealing (10 min at 700 °C, with ribbon samples sealed in a silica tube under argon) of initially fully amorphous alloy ribbons produced by chill block melt spinning using a roll speed of 30 m s^{-1}. The microstructure and d_g for selected ribbon samples were monitored by X-ray diffractometry (Bruker Advance D8 with monochromatic Cu-Kα radiation) and by transmission electron microscopy (Jeol 1200 TEM, with thin foils prepared by ion-beam thinning). The magnetic properties J_r, $_iH_c$ and $(BH)_{max}$ (computed from the B–H loop) were determined on at least 8 different samples with variable dimensions: 5–10 mm length and 20–25 μm thick, by using an Oxford Vibrating Sample Magnetometer with a maximum field of 5 T. Demagnetization field corrections were performed for M–H loops with demagnetizing factors between 0.000090 and 0.000014 corresponding to aspect ratios between 200 and 500 [18]. The reported value for magnetic properties was determined as an average, and the corresponding standard deviations were associated to the error intervals. The Curie temperature was estimated by means of magnetic thermogravimetric analysis (MTGA) with an applied magnetic field of 0.20 T. Micromagnetic simulations were performed by using time integration of the Landau–Lifshitz–Gilbert equation together with a hybrid FEM/BEM method [19] on realistic alloy models in the form of cubic structures of dimensions $100 \times 100 \times 100$ nm^3 and comprising 216 irregular grains in intimate contact, with the following intrinsic magnetic properties: $J_s^{Nd} = 1.61$ T, crystalline anisotropy $K_1^{Nd} = 4.3 \times 10^6$ J m^{-3} and exchange constant $A^{Nd} = 7.7 \times 10^{-12}$ J m^{-1} for the $Nd_2Fe_{14}B$ phase; and $J_s^{Pr} = 1.56$ T, $K_1^{Pr} = 5.6 \times 10^6$ J m^{-3} and $A^{Pr} = 12 \times 10^{-12}$ J m^{-1} for the $Pr_2Fe_{14}B$ phase [12].

3. Results

X-ray diffractograms for $Nd_{12}Fe_{82}B_6$, $RE_{12}Fe_{78}B_{10}$ and $RE_{12}(Fe_{0.9}Co_{0.1})_{76}Zr_2B_{10}$ alloys are shown in Fig. 1. All the peaks present correspond to the tetragonal $RE_2Fe_{14}B$ phase, as is expected for their stoichiometric 12 at% RE content. The same peak distribution was observed for the $RE_{12}Fe_{82}B_6$ and $RE_{12}Fe_{76}Zr_2B_{10}$ alloy samples (not shown). The mean grain sizes d_g for the complete alloy series, determined by means of the Scherrer formula for at least ten different peaks, are displayed in Table 1. A grain size refinement was observed after Pr addition (from 49 ± 7 nm to 35 ± 3 nm), followed by a general d_g coarsening for the B-enriched alloys (with the exception of the $RE_{12}Fe_{76}Zr_2B_{10}$ alloy, which in fact exhibits the smallest d_g throughout the alloy series). TEM micrographs of selected samples corresponding to $Nd_{12}Fe_{82}B_6$ and to the B-enriched $RE_{12}Fe_{78}B_{10}$ alloy ribbons are shown in Fig. 2. For the $Nd_{12}Fe_{82}B_6$ reference alloy sample (Fig. 2a) an isotropic distribution of 2/14/1 grains is manifested, with an approximate d_g value of 46 ± 4 nm, which is in good agreement with the grain size determined by XRD results (Table 1). Similar characteristics are displayed for the $RE_{12}Fe_{78}B_{10}$ alloy ribbon (Fig. 2b), with the presence of few fine precipitates (of about 10–20 nm) interspersed around the hard $RE_2Fe_{14}B$ grains as additional feature. These small crystallites would be afforded by the excess of B (probably as an iron boride [20]), thus forming a minor secondary phase with a volume fraction lower than the 5% minimum for XRD detection.

Magnetic TGA traces for the complete alloy series are displayed in Fig. 3. For the base $Nd_{12}Fe_{82}B_6$ ribbon sample, T_c was 310 °C, in accord with the reported value of 312 °C for the 2/14/1 phase [21]. A slight decrement of T_c (down to 307 °C) was recorded upon 3 at% Pr substitution, which can be associated with the lower T_c for the $Pr_2Fe_{12}B$ phase than for its $Nd_2Fe_{14}B$ counterpart [21]. The same T_c value was observed for the boron-enriched $RE_{12}Fe_{78}B_{10}$ alloy, which would imply that the excess of B is segregating outside the 2/14/1 grains. A significant reduction is exhibited for the Zr doped ribbon sample (282 °C) due to the deleterious effect

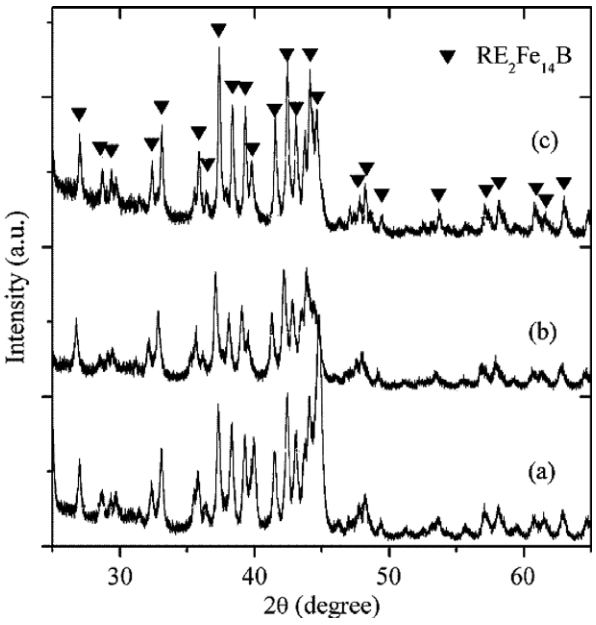

Fig. 1. X-ray diffractograms for: (a) $Nd_{12}Fe_{82}B_6$, (b) $RE_{12}Fe_{78}B_{10}$, and (c) $RE_{12}(Fe_{0.9}Co_{0.1})_{76}Zr_2B_{10}$ alloys.

Table 1
Magnetic properties of $RE_{12}Fe_{82}B_6$-based alloys ($RE = Nd_{0.75}Pr_{0.25}$) and micromagnetic data (*) for the corresponding alloy models

Alloy	${}_iH_c$ (kA m^{-1})	J_r (T)	J_s (T)	$(BH)_{max}$ (kJ m^{-3})	S	T_c (°C)	d_g (nm)	${}_iH_c^*$ (kA m^{-1})	J_r/J_s^*
$Nd_2Fe_{82}B_6$	713 ± 7	0.91 ± 0.01	1.41 ± 0.02	120 ± 4	0.47	310	49 ± 7	1042	0.61
$RE_{12}Fe_{82}B_6$	792 ± 15	0.98 ± 0.02	1.47 ± 0.02	146 ± 6	0.48	307	35 ± 3	1050	0.61
$RE_{12}Fe_{78}B_{10}$	842 ± 10	0.91 ± 0.01	1.39 ± 0.02	129 ± 3	0.53	307	43 ± 6	1082	0.61
$RE_{12}Fe_{76}Zr_2B_{10}$	1161 ± 14	0.90 ± 0.01	1.38 ± 0.03	137 ± 4	0.58	282	34 ± 3	1488	0.60
$RE_{12}(Fe,Co)_{76}Zr_2B_{10}$	1176 ± 31	0.83 ± 0.01	1.31 ± 0.02	119 ± 4	0.58	350	58 ± 6	1433	0.60

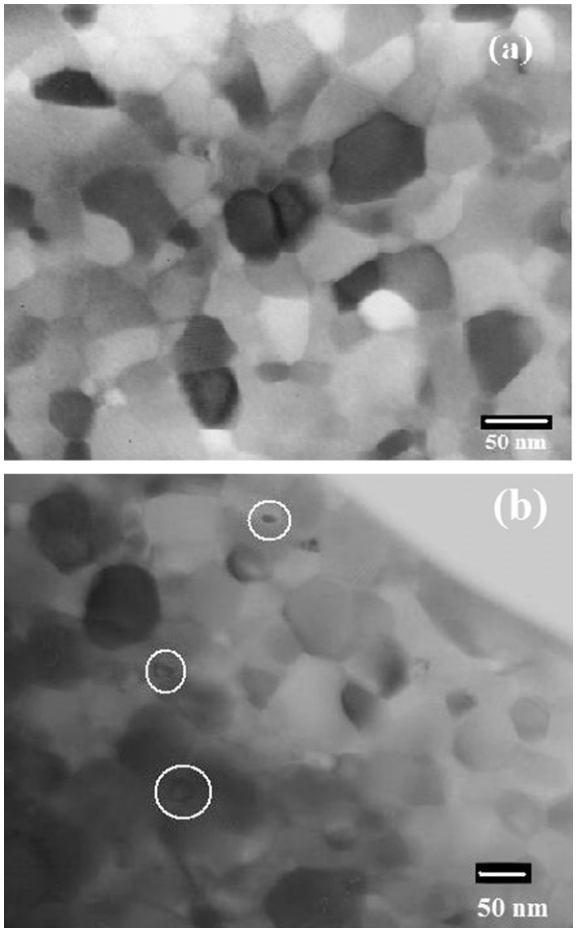

Fig. 2. TEM micrographs of selected samples corresponding to: (a) $Nd_{12}Fe_{82}B_6$ and (b) $RE_{12}Fe_{78}B_{10}$ alloys (very fine precipitates are circled in white).

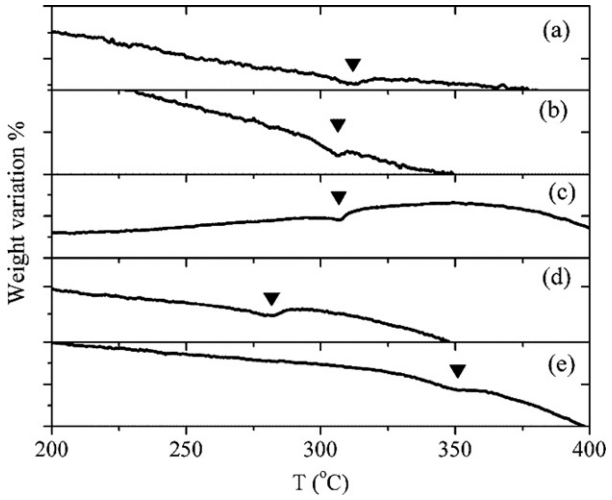

Fig. 3. Magnetic TGA traces for: (a) $Nd_2Fe_{82}B_6$, (b) $RE_{12}Fe_{82}B_6$, (c) $RE_{12}Fe_{78}B_{10}$, (d) $RE_{12}Fe_{76}Zr_2B_{10}$, and (e) $RE_{12}(Fe_{0.9}Co_{0.1})_{76}Zr_2B_{10}$ alloys.

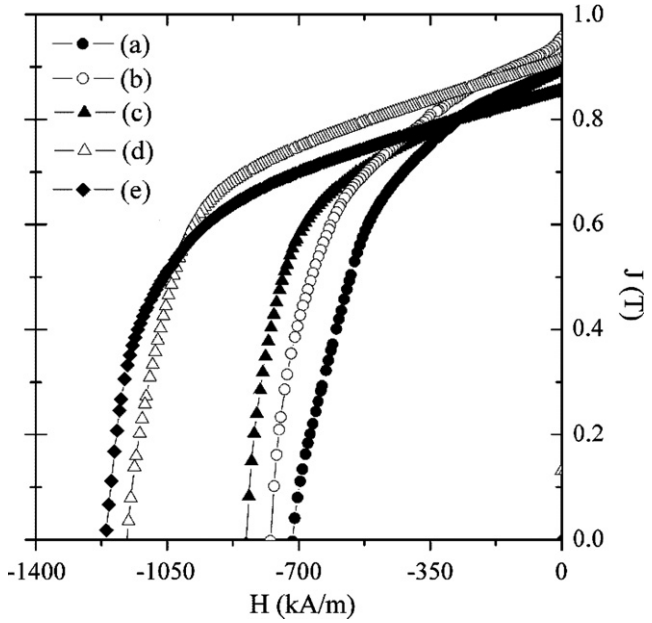

Fig. 4. Demagnetizing $J(H)$ curves for: (a) $Nd_2Fe_{82}B_6$, (b) $RE_{12}Fe_{82}B_6$, (c) $RE_{12}Fe_{78}B_{10}$, (d) $RE_{12}Fe_{76}Zr_2B_{10}$, and (e) $RE_{12}(Fe_{0.9}Co_{0.1})_{76}Zr_2B_{10}$ alloys.

of the incorporation of Zr atoms into the $RE_2Fe_{14}B$ unit cell [22,23]; this is followed by a substantial increase in T_c improvement (up to 350 °C) on partial substitution of Fe by Co, reflecting the stronger Fe–Co exchange interactions [3–5,21]. Demagnetizing J–H curves for all the alloy ribbon compositions are shown in Fig. 4, for which an increasing trend of ${}_iH_c$ is observed for the composition sequence shown in Table 1, starting at 713 ± 7 kA m^{-1} for the reference $Nd_{12}Fe_{82}B_6$ alloy, to a maximum of 1176 ± 31 kA m^{-1} for the $RE_{12}(Fe_{0.9}Co_{0.1})_{76}Zr_2B_{10}$ ribbon sample. On the other hand, the remanence exhibited an initial enhancement from 0.91 ± 0.01 to 0.98 ± 0.02 T after Pr substitution for Nd, followed by a monotonically diminishing J_r trend for the remaining compositions, to a minimum of 0.83 ± 0.01 T for the Co-containing alloy. The $(BH)_{max}$ values were 120 kJ m^{-3} for all the alloys, with a maximum of 137 ± 4 kJ m^{-3} for the $RE_{12}Fe_{76}Zr_2B_{10}$ ribbon sample.

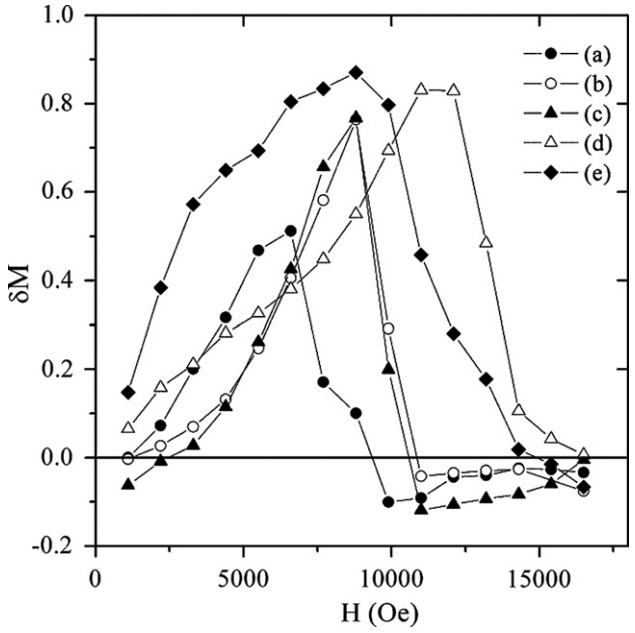

Fig. 5. Henkel $\delta M(H)$ plots for: (a) $Nd_2Fe_{82}B_6$, (b) $RE_{12}Fe_{82}B_6$, (c) $RE_{12}Fe_{78}B_{10}$, (d) $RE_{12}Fe_{76}Zr_2B_{10}$, and (e) $RE_{12}(Fe_{0.9}Co_{0.1})_{76}Zr_2B_{10}$ alloy ribbons.

The squareness S of the demagnetizing section of J–H curves, calculated as $(JH)_{max}/(J_r \cdot {}_iH_c)$ [14], displays an overall increasing tendency from 0.47 to 0.58, which contributes to maintain high-energy densities in spite of the reducing J_r values. A summary of magnetic properties is given in Table 1. Additionally, Henkel $\delta M(H)$ plots, calculated from the Wohlfarth relation $\delta M = m_d(H) - [1 - 2m_r(H)]$ (where m_d is the reduced demagnetization remanence and m_r is the reduced magnetization remanence, [9,24–26]) are displayed in Fig. 5. A predominant positive part is observed for all the alloys, reflecting the leading role of the intergranular exchange coupling over the magnetostatic interaction, which is associated with the negative deviation in the $\delta M(H)$ plot [9,24–26].

4. Discussion

The initial remanence enhancement observed upon partial replacement of Nd by Pr can be ascribed to the significant grain size refinement observed for the $RE_{12}Fe_{78}B_{10}$ alloy. The subsequent J_r diminishing tendency can be attributed to the progressive reduction in Fe content, since all the composition changes after Pr addition were effected by substitution of Fe. However, the remanence ratio $J_r/J_s \sim 0.65$ remains almost constant throughout the alloy series. The initial $(BH)_{max}$ improvement after Pr addition results from the high remanence, since $(BH)_{max}$ is proportional to J_r^2 [11,12]; while the reduced $(BH)_{max}$ observed for the B-enriched alloys are a consequence of lower remanences. In spite of these diminished J_r, the energy density remains well above 120 kJ m^{-3} for the $RE_{12}Fe_{78}B_{10}$ alloy, and even increases up to 137 kJ m^{-3} for the $RE_{12}Fe_{76}Zr_2B_{10}$ sample. This behaviour is a consequence of the improved S of the second quadrant of the J–H loop (Fig. 4, Table 1) which, in turn, results from more homogeneous and refined grain size distributions. These microstructural features are also supported by the increasing maximums observed for the Henkel plots of the alloy series, which reflect an initial enhanced intergranular exchange interaction (i.e., a higher maximum in $\delta M(H)$) after Pr addition in the reference $Nd_{12}Fe_{82}B_6$ alloy. For the Zr-doped, B-rich ribbon sample, a maximum height in $\delta M(H)$ is observed, which results from enhanced intergranular exchange coupling afforded by the reduced d_g, which also contributes for preserving same J_r values (within error intervals) as the $RE_{12}Fe_{78}B_{10}$ alloy, in spite of the reduced Fe content after Zr addition. For the Co-containing, B-rich alloy, a considerable broadening of its Henkel plot is observed, probably as a consequence of the grain size coarsening promoted by Co (Table 1). This variation of the intergranular exchange interaction and its broadening effect on $\delta M(H)$ plots has been reported previously in polycrystalline Co-based thin films [27].

On the other hand, the initial increment of ${}_iH_c$ for the Pr substituted alloy (relative to the $Nd_{12}Fe_{82}B_6$ sample) can be ascribed to a higher K_1 constant, afforded by the incorporation of Pr atoms into the 2/14/1 crystal structure, as it is confirmed by the reduced T_c value of this alloy. Concerning the B-enriched alloys, the ${}_iH_c$ improvement recorded for $RE_{12}Fe_{78}B_{10}$ alloy (with respect to the $RE_{12}Fe_{82}B_6$ sample) can be explained on the basis of the grain size coarsening observed after B enrichment (which causes a concomitant noticeable reduction in J_r, with respect to the $RE_{12}Fe_{82}B_6$ alloy, Table 1) and on the interaction of secondary phases with the nucleation of reverse domains process, as it is described in the next paragraph. The observed ${}_iH_c$ enhancement after Zr addition is in accord with previous reports for $Nd_{12}Fe_{82-x}Zr_xB_6$ alloys [22,28], for which higher anisotropy fields H_A were reported as a result of the replacing of Nd atoms by Zr within the $RE_2Fe_{14}B$ unit cell [22,23]. This introduction of Zr into the 2/14/1 cell is also reflected by the considerable reduction in T_c determined for the $RE_{12}Fe_{76}Zr_2B_{10}$ alloy sample (See Table 1). Finally, although the $RE_{12}(Fe_{0.9}Co_{0.1})_{76}Zr_2B_{10}$ alloy sample exhibits a slight improvement in ${}_iH_c$ ($\sim$1.2%) relative to the $RE_{12}Fe_{76}Zr_2B_{10}$ ribbon, the difference is barely significant, considering the experimental uncertainty in measurements. The interesting point here is that, according to previous reports, the addition of Co to $Nd_{12}Fe_{14}B_6$ alloys decreases the H_A, which, in fact, leads to reduced ${}_iH_c$ values [3,4,21,22]. This implies, for the present case, that the Zr addition, together with the increased mean grain size promoted by Co, are able to counterbalance the deleterious effect of the Co substitution on H_A with a concomitant beneficial T_c increment (up to 350 °C, Table 1).

Micromagnetically simulated J–H curves are shown in Fig. 6 for all the alloys in the series. For the initial $Nd_{12}Fe_{82}B_6$ alloy model, an ${}_iH_c$ of 1042 kA m^{-1} was observed, which is considerably larger (46%) than the experimental value, due to the fact that the cubic alloy model assumes the ideal nucleation field for reverse domains corresponding to a perfect grain structure without

defects. Nevertheless, the simulated J–H plot reflects the intergranular exchange coupling, with a J_r/J_s ratio (0.61) very similar to the measured J_r/J_s (of 0.64). Although consistently higher ${}_iH_c$ values were obtained for the remaining alloy models relative to the corresponding experimental values, a progressive ${}_iH_c$ enhancement equivalent to the increasing sequence displayed in Table 1 was attained by assuming, for the alloy models, the same experimentally observed microstructural and intrinsic magnetic properties variations. Firstly, the initial Pr substitution was simulated by means of a linear interpolation of the intrinsic properties of $Nd_2Fe_{14}B$ and $Pr_2Fe_{14}B$, which mimics the compositional variation, i.e., $K_1 = 0.75K_1{}^{Nd} + 0.25K_1{}^{Pr} = 4.62 \times 10^6\ J\ m^{-3}$ and correspondingly, $J_s = 1.59$ T, $A = 8.77 \times 10^{-12}\ J\ m^{-1}$. In this way, a primary ${}_iH_c$ improvement was observed. Further increase in ${}_iH_c$ for the B-enriched $RE_{12}Fe_{78}B_{10}$ alloy model was attained by assuming the presence of magnetic Fe_3B grains ($K_1 = -3.22 \times 10^5\ J\ m^{-3}$, $J_s = 1.62$ T, $A = 1.25 \times 10^{-11}\ J\ m^{-1}$) as secondary phase, which, according to Ref. [20], are expected to form as a consequence of the excess content of B. This secondary phase was included within the magnetic model as a volume fraction of 2%, which is lower than the detection limit of the XRD analysis (~5%). This alloy model showed an ${}_iH_c$ enhancement of 3% with respect to the stoichiometric $RE_{12}Fe_{82}B_6$ composition, which is similar to the 6% experimentally determined (Table 1). This ${}_iH_c$ improvement can be partially associated to the effect of the secondary grains on the nucleation of reverse domains, as it is shown in Fig. 7a, for which the equilibrium magnetization distribution for the $Nd_{12}Fe_{82}B_6$ alloy model at $H = -398\ kA\ m^{-1}$ exhibits the beginning of the magnetization reversal for some few spins along the grain boundary (circled in white), where the competition between magnetocrystalline anisotropy and the exchange interaction affords the rotation of the magnetization away of the grain easy axis [12,29–31]. In Fig. 7b, the onset of magnetization

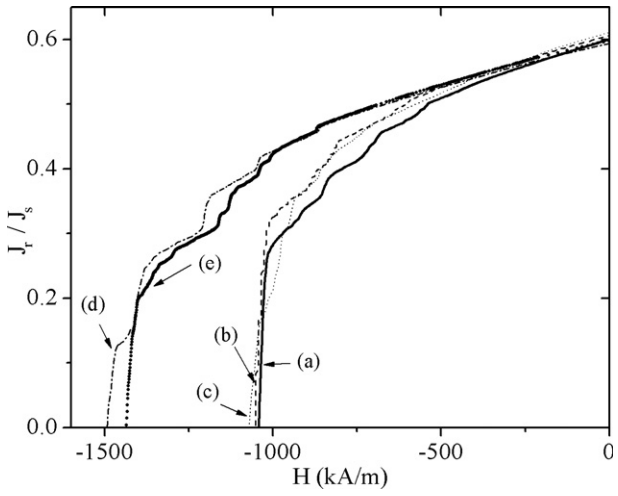

Fig. 6. Micromagnetically simulated J(H) curves for: (a) $Nd_2Fe_{82}B_6$, (b) $RE_{12}Fe_{82}B_6$, (c) $RE_{12}Fe_{78}B_{10}$, (d) $RE_{12}Fe_{76}Zr_2B_{10}$, and (e) $RE_{12}(Fe_{0.9}Co_{0.1})_{76}Zr_2B_{10}$ alloy models.

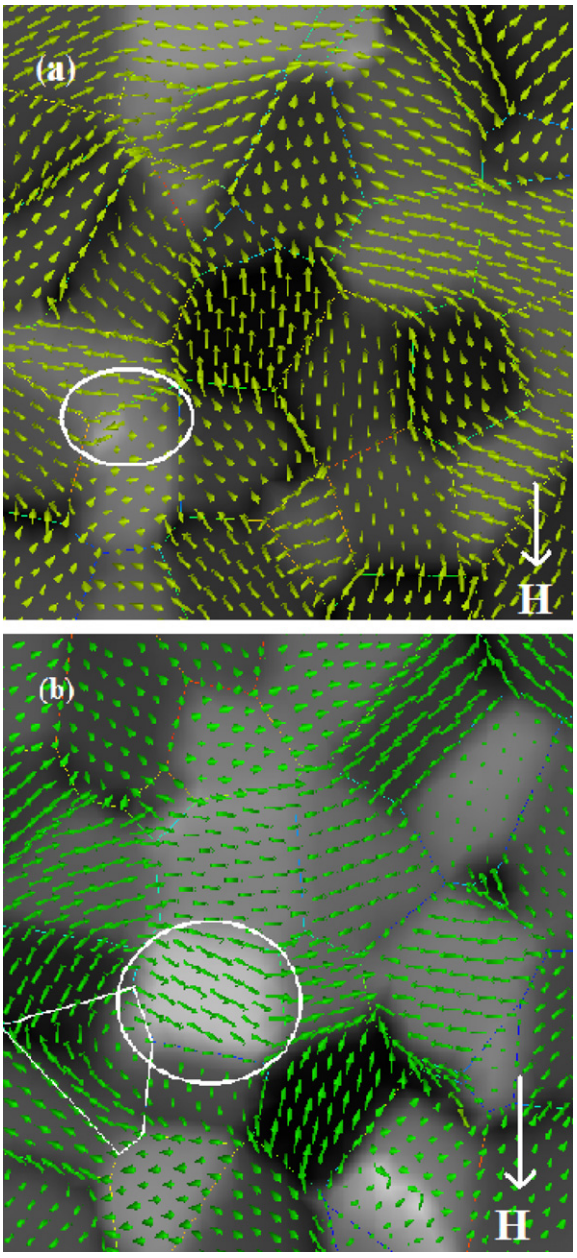

Fig. 7. Magnetization distribution for: (a) $Nd_2Fe_{82}B_6$ alloy model (at $H = -398\ kA\ m^{-1}$) and (b) $RE_{12}Fe_{78}B_{10}$ alloy model (at $H = -485\ kA\ m^{-1}$). The cube model shows a (100) face, with the magnetic field H applied along the z direction.

reversal for the $RE_{12}Fe_{78}B_{10}$ alloy model starts at a higher field ($H = -485\ kA\ m^{-1}$), within a hard grain (circled in white) adjacent to a secondary phase grain (whose shape is white labelled) which exhibits a vortex-like spin configuration. This alloy model does not include the grain-size coarsening observed for the $RE_{12}Fe_{78}B_{10}$ alloy (Table 1), which has also an influencing role in achieving high values of ${}_iH_c$ [12–14]. Additionally, comparable J_r/J_s enhancement was obtained (Table 1).

For the $RE_{12}Fe_{76}Zr_2B_{10}$ composition, the same $RE_{12}Fe_{78}B_{10}$ alloy model was used but with modified intrinsic magnetic properties. The variations of K_1, J_s and A were estimated from experimental reports of Zr substi-

tuted Nd–Fe–B and Pr–Fe–B alloys [22] as follows: higher K_1 constant (5.71×10^6 J m^{-3}, calculated from an enhancement of 23.8% of the anisotropy field H_A) and decreased J_s and A values (1.56 T and 8.57×10^{-12} J m^{-1}, respectively, estimated from reductions of –1.56% in J_s and of –2.17% in T_c). These modified intrinsic parameters led to an $_iH_c$ enhancement of 37.5% (relative to the $RE_{12}Fe_{78}B_{10}$ alloy model), which was very close to the experimental value of 38.0% determined from Fig. 4 (see Table 1). Finally, for the co-containing composition, reduced K_1 values, relative to the $RE_{12}Fe_{76}Zr_2B_{10}$ alloy model ($K_1 = 5.58 \times 10^6$ J m^{-3}, calculated from an H_A reduction of –2.25%) with concurrent J_s and A increases (1.57 T and 9.83×10^{-12} J m^{-1}, respectively, estimated from increments of 0.52% and 14.6% in J_s and T_c, respectively) were assumed, based also on experimental reports [22,32,33]. An effective decrease in $_iH_c$ of –3.6% with respect to the $RE_{12}Fe_{76}Zr_2B_{10}$ alloy model was predicted, preserving a J_r/J_s enhancement of 0.60, comparable to the experimental $J_r/J_s = 0.63$ (Table 1). This disagreement in calculated coercivity values with the experimental data can be ascribed again to the grain-size coarsening observed after Co addition (Table 1), since a coarser d_g distribution plays an important role in preserving high values of $_iH_c$ [12–14], in a concomitant way to the intrinsic magnetic property variations proposed for the corresponding alloy model.

5. Conclusion

Considerable enhancement of intrinsic coercivity (between 50% and 65%) in $RE_{12}Fe_{82}B_6$-base melt-spun alloys (RE = Nd, Nd + Pr) is attainable by means of excess of B content (up to 10 at%) and Zr–Co additions, together with excellent J_r values (>0.90 T) and useful energy densities over 120 kJ m^{-3}.

Acknowledgements

I. Betancourt is grateful for the award of a scholarship for a sabbatical leave by DGAPA-UNAM. I. Betancourt also acknowledges to Leticia Baños, Gabriel Lara, Carlos Flores, and Esteban Fregoso for their valuable technical assistance.

References

[1] Croat JJ, Herbst JF, Lee RE, Pinkerton FE. J Appl Phys 1984;55:2078.
[2] Sawaga M, Fujimura S, Tagawa M, Yamamoto H, Matsuura Y. J Appl Phys 1984;55:2083.
[3] Hadjipanayis GC, Liv JF, Gabay A, Marinescu M. Current status of rare-earth permanent magnet research in USA. In: Proceedings of 19th international workshop on rare earth permanent magnets and their applications. Beijing: Journal of Iron and Steel Research; 2006. p. 2.
[4] Hirosawa S. Magnets: remanence enhanced. In: Buschow KHJ, editor. Concise encyclopedia of magnetic & superconducting materials. Amsterdam: Elsevier; 2005. p. 877.
[5] Jiles DC. Acta Mater 2003;51:5907.
[6] Skomski R, Coey JMD. Permanent magnetism. New York: Taylor & Francis Group; 1999. p. 303.
[7] du Tremolet de Lacheisserie E, Ochette PR. In: du Tremolet de Lacheisserie E, editor. Magnetism. Materials and applications. New York: Springer; 2003. p. 433.
[8] Zhao CS, Dong DL. Clinical observation of rare-earth magnetic acne-remedial beauty mask with Chinese medicine in treatment for acne. In: Kaneko H, Homma M, Okada M, editors. Proceedings of 16th international workshop on rare Earth magnets and their applications. Sendai: The Japan Institute of Metals; 2000. p. 1103.
[9] Liu W, Liu Y, Skomski R, Sellmyer DJ. Nanostructured exchange-coupled magnets. In: Liu Y, Sellmyer D, Shindo D, editors. Handbook of advanced magnetic materials. New York–Beijing: Tsinghua University Press–Springer; 2006. p. 226.
[10] Kramer MJ, Lewis LH, Tang Y, Dennis KW, McCallum RW. Scripta Mater 2002;47:557.
[11] Kronmuller H, Fischer R, Seeger M, Zern A. J Phys D: Appl Phys 1996;29:2274.
[12] Kronmuller H, Fahnle M. Micromagnetism and the microstructure of ferromagnetic solids. Cambridge: Cambridge University Press; 2003. p. 90.
[13] Davies HA. J Magn Magn Mater 1996;157/158:11.
[14] Goll D, Seeger M, Kronmuller H. J Magn Magn Mater 1998;185:49.
[15] Mendoza G, Davies HA. J Alloys Compd 1998;281:17.
[16] Davies HA, Betancourt JI, Harland CL. Scripta Mater 2001;44:1337.
[17] Okada M, Sugimoto S, Ishizaka C, Tanaka T, Homma M. J Appl Phys 1985;57:4146.
[18] Bozorth RM. Ferromagnetism. Piscataway: IEEE Press; 1978. p.849.
[19] Fidler J, Schrefl T. J Phys D: Appl Phys 2000;33:R135.
[20] Chang HW, Chang WC, Ho JC, Hikal WM, Hamdeh HH. Physica B 2003;327:292.
[21] Herbst JF. Rev Mod Phys 1991;63:819.
[22] Jurczyk M, Wallace WE. J Magn Magn Mater 1986;59:L182.
[23] Capehart TW, Mishra RK, Pinkerton FE. J Appl Phys 1993;73:6476.
[24] Henkel O. Phys Stat Sol 1964;7:919.
[25] Bertotti G. Hysteresis in magnetism. San Diego: Academic Press; 1998. p.250.
[26] Garcia-Otero J, Porto M, Rivas J. J Appl Phys 2000;87:7376.
[27] Kelly PE, ÓGrady K, Mayo PI, Chantrell RW. IEEE Trans Magn 1989;25:3881.
[28] Betancourt JI, Davies HA. IEEE Trans Magn 2001;37:2480.
[29] Schrefl T, Fidler J, Kronmuller H. Phys Rev B 1994;49:6100.
[30] Fischer R, Kronmuller H. Phys Rev B 1996;54:7284.
[31] Rong C, Zhang H, Chen R, He S, Shen B. J Magn Magn Mater 2006;302:126.
[32] Abache C, Oesterreicher H. J Appl Phys 1986;60:1114.
[33] Grossinger R, Krewenka R, Sun XK, Eibler R, Kirchmayr HR, Buschow KHJ. J Less-Comm Met 1986;124:165.